Available online at www.sciencedirect.com
SCIENCE DIRECT®
International Journal of Heat and Mass Transfer 47 (2004) 5685–5702
International Journal of HEAT and MASS TRANSFER
www.elsevier.com/locate/ijhmt

Measurements and modeling of the flow and heat transfer in a contoured vane-endwall passage

Hugo D. Pasinato [1], Kyle D. Squires, Ramendra P. Roy *

Mechanical and Aerospace Engineering Department, Arizona State University, Box 876106, Tempe, AZ 85287-6106, USA

Received 26 December 2003; received in revised form 8 July 2004
Available online 25 September 2004

Abstract

Numerical simulations and laboratory measurements are obtained of the flow field and heat transfer in a linear cascade of turbine vanes, with and without secondary air injection through three discrete angled slots upstream of each vane. The hub endwall is axially profiled while the tip endwall is flat, with the hub endwall the focus of heat transfer investigation. Experimental measurements are compared to predictions of the steady-state flow obtained from solution of the Reynolds-averaged Navier–Stokes equations. Surface heat transfer characteristics predicted in the simulations are similar to measured values, with the most significant differences occurring in the cooling effectiveness.

1. Introduction

The flow and thermal fields within gas turbine components are complex and continue to challenge measurements and computational models. Geometric complexity is inherent to most configurations and advances in the fundamental knowledge base that might eventually improve predictive capabilities provide motivation for component studies. The flow and heat transfer in and around vane-endwall passages is an example central to the present effort in which geometrical aspects of the configuration substantially complicate fields. The development of a horseshoe vortex due to the rolling up of boundary layer fluid around the leading edge of the vane is a well-known structural feature that can strongly influence the endwall heat transfer and distribution of losses throughout the passage. In addition, there are in many configurations, slots, steps, and/or gaps, for example, that distort the flow and heat transfer in unpredictable ways. In some instances, distortions are purposefully introduced in order to achieve an effect, e.g., as with endwall contouring and/or the use of film cooling. In many other instances, perturbations to the flow are unintentional, e.g., as might result from aspects of the manufacturing process.

There has been a relatively large body of previous work focusing on effects that can influence either the flow or heat transfer within vane passages (e.g., see [1] for a general review). Vane-endwall configurations blend several effects such as complexities of turbulent flows subject to strong perturbations in pressure gradient and streamline curvature, cross-flow coolant injection, large-scale secondary flow, and possibly unsteadiness, among other effects. Coolant injection, for example, increases the complexity of the overall flow field by the

* Corresponding author. Tel.: +1 480 965 1482; fax: +1 480 963 1384.
E-mail address: roy@asu.edu (R.P. Roy).
[1] Present address: Departmento de Mecanica, Facultad de Ingenieria, Universidad Nacional de la Patagonia San Juan Bosco, 9000 Comodoro Rivadavia, Argentina.

0017-9310/$ - see front matter © 2004 Elsevier Ltd. All rights reserved.
doi:10.1016/j.ijheatmasstransfer.2004.07.032

Nomenclature

δ_2	boundary layer momentum thickness
δ_{99}	boundary layer thickness
η	cooling effectiveness
ω	specific turbulence dissipation rate
Ω_{ij}	mean rotation rate
ρ	fluid density
ξ_j	coordinate along the plane S_j, $j = 1$ or 2
BR	blowing ratio
C	true chord length
c_f	skin friction coefficient
c_p	specific heat at constant pressure
C_{ax}	axial chord length
C_{p0}	total pressure loss coefficient
H	boundary layer shape factor
k	turbulence kinetic energy
P	vane pitch
P_0	total pressure
q''_w	wall heat flux
R	leading edge radius
Re_{δ_2}	momentum thickness Reynolds number
S_{ij}	mean strain rate
St	Stanton number
T_∞	freestream temperature
T_r	reference temperature (adiabatic wall temperature)
T_s	secondary air temperature
T_w	wall temperature
u	streamwise velocity component
U_∞	freestream velocity
U_{avg}	mixed-mean streamwise velocity component
v	pitchwise velocity component
V_{avg}	mixed-mean pitchwise velocity component
x	streamwise (axial) coordinate
y	pitchwise coordinate
z	spanwise coordinate

vortical interactions of the injected fluid and outer flow in the vicinity of the injection location. Details of the characteristics of the injection have been shown in previous studies to depend on factors related to specific details of hole geometries, velocity ratio, density ratio, and plenum effects e.g., see [2–7].

Some studies have used experimental measurements or numerical simulations to study particular effects, but without the introduction of geometric complexity. A representative contribution in this area is the work of Jung and Lee [5], who measured the effect of coolant injection through cylindrical holes into a flat plate boundary layer, using a constant inclination angle of 35° and several horizontal orientation angles with respect to the streamwise direction of the external flow. Injection velocity ratios of 0.5, 1, and 2 were used. It was found that the mixing between the freestream fluid and coolant increased as the orientation angle increased, and as the injection velocity ratio increased. The surface heat transfer increased as a result.

Wilfert and Wolff [6] studied the effect of the injection flow supply conditions and plenum geometry on film cooling effectiveness in a flat plate boundary layer. An array of cylindrical holes were used, inclined at 30° degrees to the external flow. The hole spacing in the lateral direction was fixed, and the hole length-to-diameter ratio was varied. In addition, ribs were used in the supply channel to redirect and improve the inflow to the holes. The film cooling effectiveness was measured for variations in the blowing ratio from 0.5 to 1.25. Wilfert and Wolff [6] found that there can be significant effects on the flow field in the near-hole region, similar conclusions were reached by Hale et al. [7] in a related study.

Strategies to overcome the aerodynamic losses arising from secondary flows have included the use of endwall profiling and/or secondary air injection to alter the underlying vortical flow within a passage e.g., see [8–12]. Duden et al. [8] applied axisymmetric profiling to an endwall and found that the extent of the secondary flow was reduced as well as the secondary-flow losses. In two companion works, Harvey et al. [11] and Hartland et al. [12] have presented the design and experimental validation of a passage subject to non-axisymmetric endwall profiling. Reynolds-averaged CFD models employed in this study predicted a reduction in secondary flow, but with small overall reduction in losses.

Recent experimental works relevant to the current contribution include that reported by Oke et al. [13] in which experiments were carried out in a linear cascade comprised of three vanes and two endwalls. One endwall was flat and the other contoured from upstream of the leading edge, the contour continuing through the passage. The incoming flow was of high turbulence and large length scale, in an attempt to model typical engine combustor exit flows. Film cooling air was introduced through two rows of slots at the contoured endwall, the slots in one row could have a specific pitchwise area distribution. The objective was to determine whether the secondary flows could be used to control the pitchwise coolant distribution in and around the passage. Two parameters were varied in the experiments. The first was the coolant-to-main flow momentum flux ratio. The other was the slot area distribution in one of the rows. These investigators found that at low momentum flux ratios the coolant migrated towards the suction side.

At higher ratios the pressure side endwall region was cooled more effectively.

Ames et al. [14] examined the effect of aeroderivative combustor turbulence on endwall heat transfer distributions. Measurements were performed in a large-scale linear cascade at low speed conditions. The inlet turbulent intensity (Tu) was varied from 0.7% to 14%. At low Tu, the endwall heat transfer exhibited the influence of the three-dimensional flow field, this influence was less evident in the high Tu cases. The boundary layer and turbulence characteristics of the main flow were measured across one vane passage at a plane approximately 0.3 axial chord length upstream of the vane leading edge for three Reynolds numbers and both low and high Tu. A single-hot wire probe was used for these measurements. Peak velocity, boundary layer thickness, skin friction coefficient, and Tu were obtained. The data indicates that for the cases with high freestream turbulence intensity, the maximum in the freestream velocity was higher in the vicinity of the vane leading edge and lower near the mid-pitch. The boundary layer thickness and momentum thickness had the opposite trend, i.e., larger thicknesses were measured near the mid-pitch compared to the vicinity of the vane leading edge.

1.1. Focus of the current contribution

In an earlier work, Pasinato et al. [15] (referred to as PSR throughout) reported experimental measurements and predictions of the flow and thermal fields in a linear vane cascade with flat hub and tip endwalls. The focus of the investigations was prediction of the thermal signature on the hub endwall and interpretation of the solutions by eduction of the coherent structures predicted in the numerical simulations using the technique of Jeong and Hussain [16]. Three Reynolds-averaged Navier–Stokes (RANS) models were applied, the Spalart–Allmaras [17] one-equation model, RNG k–ε model [18], and a full Reynolds stress transport closure [19], each model integrated all the way to the wall, i.e., wall functions were not employed. These models offered varying degrees of complexity for closure of the Reynolds stress in the momentum equations, the Spalart–Allmaras and RNG k–ε models using scalar eddy viscosity while the full Reynolds stress closure does not require alignment between the turbulent stress and mean strain rate. A constant turbulent Prandtl number was employed for prediction of the turbulent heat flux by each of the models. In general, while the more complex Reynolds stress closure does not force alignment between the turbulent stress and mean strain rate and can, for example, account for Reynolds stress production due to anisotropy in the normal stresses, the predictions of the velocity and temperature fields obtained using the three models and reported in PSR were not substantially different. The calibration range of scalar eddy viscosity models is sufficiently broad to predict to useful accuracy boundary layer growth upstream of the vanes, in turn providing part of the explanation for the similar quality of predictions obtained from the models. The similar predictions yielded similar vortical structures (e.g., the horseshoe vortex) as obtained using the full Reynolds stress model and comparable heat transfer distributions near the leading edge of the vane and within the passage. Also investigated in PSR was the application of secondary air injection through three angled slots that were positioned in the flat hub endwall upstream of the vane leading edge and used to alter the flow structure and in turn endwall transfer rates. Introduction of secondary air strongly altered the flow near the vane leading edge, with substantial regions of the endwall characterized by elevated values of cooling effectiveness.

The present contribution extends the work reported in PSR by focusing on the effect of axial profiling of the hub endwall. As shown below, because of the axial profiling the streamwise development of the flow is subject to relatively strong distortion, sufficient to cause flow separation upstream of the leading edge of the vane. The primary objective of the present contribution is to characterize the flow and thermal fields using measurements and predictions obtained from the RANS equations, one of the areas of interest being to elucidate the main features of the flow and contrast them against the earlier work on the flat hub endwall reported by PSR. Analogous to PSR, secondary air injection is employed as a means to alter heat transfer characteristics in the vicinity of the vane leading edge As also shown below, while secondary air injection can favorably alter endwall heat transfer distributions near the vane leading edge, the mechanisms are quite different compared to the companion flat endwall case. In addition, a broader range of experimental measurements are acquired in the present investigation compared to PSR, enabling a more thorough characterization of the flow, including measurements of the total pressure loss coefficient.

Following in the next section is a brief summary of the experimental facility and instrumentation. Only the salient features that differ from the work reported by PSR are reported. The computational procedures are also described, including a description of the flow solver, approach to grid generation, and turbulence model. The flow and thermal fields are then described, using both the measured and predicted characteristics of: the mean flow and turbulence intensities upstream and downstream of the passage, heat transfer on the endwall (Stanton number and cooling effectiveness for a baseline case and two blowing ratios), as well as measurements and predictions of the total pressure loss coefficient. The measurements are used to assess the numerical simulations, the flow structure predicted in the computations is also employed to assist in contrasting the current results against the results of PSR.

Finally, some of the figures which follow appear in gray-scale. A version of the manuscript with color figures can be downloaded from http://www.fulton.asu.edu/~squires/publications.html.

2. Approach

2.1. Experimental configuration and measurement techniques

Measurements were obtained in the same open-circuit wind tunnel as used in the investigations reported by PSR and the reader is referred to that work for details on the tunnel configuration. Similar to PSR, a linear vane cascade was considered, the cascade comprised of five acrylic vanes scaled up from an actual engine inlet vane configuration by a factor of 6.6. The vane geometry is an untwisted version which follows the mid-span shape of the engine vane. Geometric details of the vanes used in the experiments are provided in Table 1.

Fig. 1a–c schematically show a portion of the vane cascade, the axially profiled acrylic hub endwall, and the secondary air injection slots. As shown in the figures, secondary air injection occurs slightly upstream of the vane leading edge. The slots are embedded in a 'notch' with the injected air roughly tangent to the endwall contour as shown. Experiments and simulations with air injection were performed for blowing ratios of 1.3 and 1.7.

The upstream boundary layers on the hub and tip endwalls are removed by adjustable bleeds at knife edges (one on each wall), the location of the bleed on the tip endwall being closer to the vane cascade inlet plane. A trip wire was installed 25.4 mm downstream from the hub endwall knife edge, the resulting hub endwall turbulent boundary layer was measured at three pitchwise locations in the cascade inlet plane 170 mm upstream of the vane leading edge (c.f., Fig. 1a).

The streamwise (x component) and pitchwise (y component) velocities were measured using a two-component LDV system (TSI) consisting of a 300 mW Argon-Ion laser and a fiberoptic probe with 50 mm beam spacing and a backscatter light detector. A 261 mm focal length transmitting lens was used for the measurements. The LDV probe volume in air was calculated to be an ellipsoid with minor axis (in the streamwise direction) about 0.1 mm long and major axis (in the spanwise direction) about 1.0 mm long. The two beam pairs (green and blue) functioned in the random mode to enable high data rates. A three-axis traverse mechanism with a rotating stage served as the LDV probe mount.

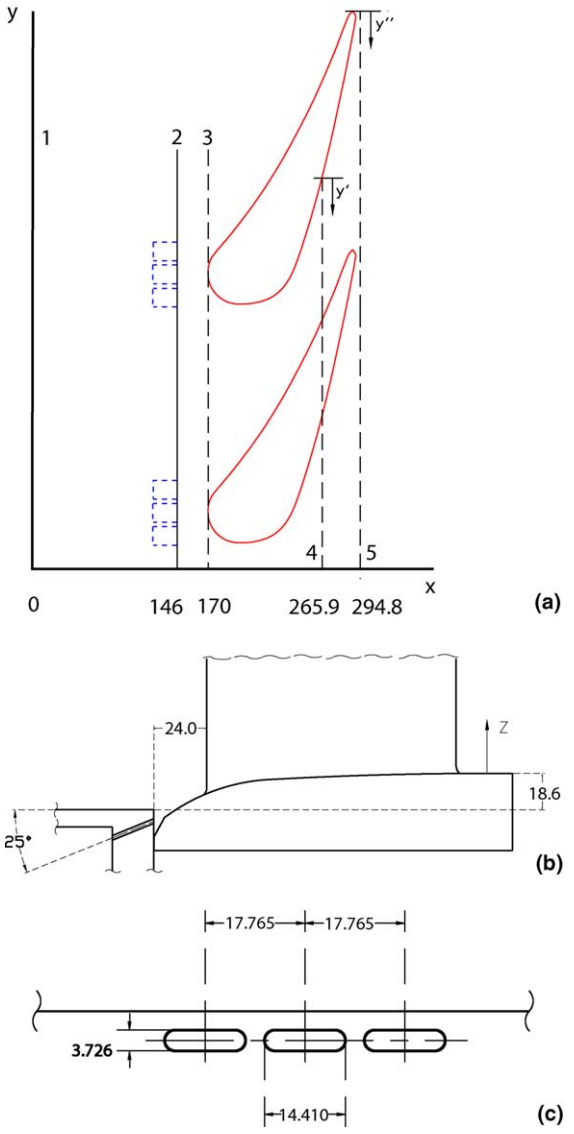

Fig. 1. (a) Top view of the vane configuration. (b) Side view of the hub endwall and slots for secondary air injection. (c) End view facing the slots. Dimensions in millimeters. In (a): Plane 1: inlet; Plane 2: secondary air injection; Plane 3: leading edge; Plane 4 and Plane 5: C_{p0} measurement planes.

Table 1
Stator vane geometry

True chord length, C	244 mm
Axial chord length, C_{ax}	115.5 mm
Pitch, P/True chord length	0.768
Span@Inlet	210.2 mm
Span@Exit	200.7 mm
Inlet angle, Exit angle	0°, 75°
Leading edge radius, R	24.2 mm
Pitch	187.3 mm

Since the wind tunnel was an open-circuit one, solid particles could not be used for seeding the air flow. Instead, a water mist with droplet size no larger than 2 μm, created by six venturi nozzles, was utilized. Of the six nozzles, four were oriented vertically and two horizontally in a plane immediately downstream of the turbulence generator (the turbulence generator was placed 838 mm upstream of the vane leading edge plane).

Three sets of velocity measurements were acquired and are reported in the following section:

- Spanwise variation of the streamwise velocity in the x–z plane 170 mm upstream of the vane leading edge. The streamwise mean velocity was measured at three pitchwise locations, $y/P = -0.5$, -0.75, and -1.0 (c.f., Fig. 2). These inlet plane velocities were used to establish the inflow conditions of the computations.
- Pitchwise variation of the streamwise and pitchwise velocities upstream of the vane leading edge in two x–y planes. The wall-normal distances of the planes from the hub endwall were 55 mm and 100 mm (both outside the boundary layer), the streamwise positions of measurement were 50 mm and 10 mm upstream of the vane leading edge (c.f., Fig. 2).
- Pitchwise variation of the streamwise and pitchwise velocities in two x–y planes downstream of the vane trailing edge. The wall-normal distances of the planes from the hub endwall were 55 mm and 100 mm, the streamwise positions of the measurements planes were 10 mm and 20 mm downstream of the vane trailing edge.

In addition to measurements of the velocity field that were used to document the flow and provide one assessment of the computations, losses were quantified using measurements of the total pressure. Two different miniature Kiel probes were used for the total pressure measurements. A probe with a straight impact tube was used to obtain the pitchwise-spanwise pressure maps 9.3 mm downstream from the vane trailing edge and 9.5 mm upstream from the vane leading edge. A probe with a bent impact tube was used to obtain such a pressure map in the vane passage 95.7 mm downstream from the leading edge, the bent tube enabling measurement to 1 mm from the vane suction surface.

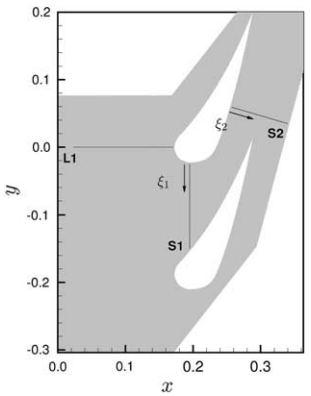

Fig. 2. Position of planes for results in Fig. 3 and visualizations shown in Figs. 6–8. Local coordinates ξ_i normal to the vane suction surface as shown. Axes dimensions in meters.

Heat transfer distribution on the hub endwall was measured using the same transient thermochromic liquid crystal (TLC) technique as reported in PSR, except that the TLC transition (70% green intensity) temperature was 311.4 K as determined by calibration. Similar to the experiments on the flat endwall reported by PSR, the entire hub endwall surface area of interest was not imaged during any one experiment. Instead, three subregions with significant overlap between them were imaged during three separate experiments—the regions being that around the leading edge, on the vane suction side, and on the vane pressure side. For each region, the illumination which must be homogeneous and the camera view were optimized. The results presented combine those from the three regions.

The mainstream air was heated to between 320.1 K and 321.3 K for the experiments. In each secondary air injection case, two experiments were required for determining the convective heat transfer coefficient (Stanton number) and cooling effectiveness distributions, the difference between the two experiments being the secondary air temperature (316.9 K and 324.6 K for BR = 1.3, 318.8 K and 326.7 K for BR = 1.7).

The uncertainty in the measured convective heat transfer coefficient is ±8% over most of the endwall. That in the cooling effectiveness is ±10%. However, since one-dimensional semi-infinite medium formulation of transient heat conduction was used for the hub endwall, higher uncertainty (≈12%) in the results should be expected near the vane-endwall junction.

2.2. Simulation overview

Predictions of the fluid flow and heat transfer were obtained from numerical solution of the Reynolds-averaged Navier–Stokes (RANS) equations. The turbulent stress and turbulent heat flux appearing in the RANS equations and thermal energy equation were closed using the Spalart–Allmaras [17] one-equation turbulence model and a constant turbulent Prandtl number (=0.9), respectively. The Spalart–Allmaras model relates the turbulent stress to the mean strain rate via isotropic eddy viscosity. Application of the model is further motivated by the fact that it often yields predictions of comparable accuracy to those obtained from more sophisticated closures, one of the findings reported in PSR.

The solutions for the incompressible flows considered in this study were obtained using Fluent [20]. The numerical method is based on a finite-volume approach that is second-order accurate in space. The SIMPLEC method [21] is used for the pressure-velocity coupling. The resulting system of algebraic equations are solved using a segregated iterative approach. Convergence of the discretized system was monitored using the local mass residual, i.e., the maximum imbalance of the mass in any control volume at any iteration. Residuals from the other transport equations (momentum, thermal energy, and turbulence transport equations) were typically smaller than those from conservation of mass. For convergence of the continuity equation to 10^{-8}, approximately 4000 iterations were required.

Computations were performed using unstructured meshes comprised of hexahedra and prisms that were created using Gambit [20]. A series of four meshes were created in order to investigate grid convergence, the resolutions ranging from the coarsest grid comprised of 2.7×10^5 cells to the finest mesh of 2.7×10^6 cells. Based on the friction velocity at the inlet, for each grid the first cell center was within one viscous unit of the endwall. Convergence in the skin friction and Stanton number with the grid is demonstrated in the Planes L1 and S2 in Fig. 3 (the positions of these planes are shown in Fig. 2). Fig. 3 shows that in the L1 plane (upper row of frames in the figure) the skin friction and Stanton number upstream of the vane exhibit adequate grid convergence, differences only apparent on the coarsest mesh. In Plane S2 (lower row of frames in the figure), the coarser meshes show that C_f and St levels are below those on the finer meshes. As also observed in Plane L1, there is almost no difference in C_f and St on the two finest meshes, showing convergence for the finest resolutions used. Results presented below were obtained on the finest mesh of 2.7×10^6 cells.

The slots through which secondary air was introduced were included in the computational domain (e.g., see Fig. 6). This allowed non-uniformities in the exiting flow to be partially accounted for by the computational model, though without a complete inclusion of the supply plenum the present approach remains approximate. For the incompressible flow considered in this work, the blowing ratio, BR, reduces to the ratio of the uniform inlet velocity at the entrance to the slot normalized by the freestream velocity at the inlet to the computational domain. Blowing ratios of 1.3 and

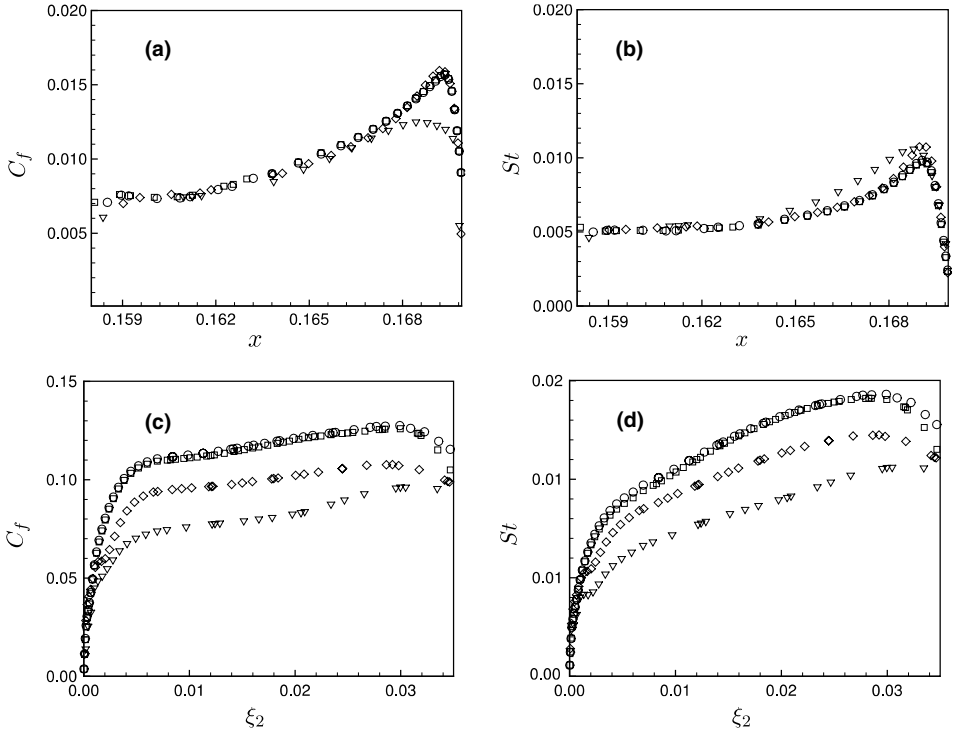

Fig. 3. Influence of the mesh on the skin friction and Stanton number in Plane L1 (upper row) and in Plane S2 (lower row), baseline case. (□) 2.7×10^6 cells; (○) 1.4×10^6 cells; (◇) 8×10^5 cells; (▽) 2.7×10^5 cells. Axis dimensions in meters. (a, c) Skin friction; (b, d) Stanton number.

1.7 were considered in the calculations with secondary air injection (the same values as in the experiments with air injection).

The experimental measurements of the streamwise mean velocity from the three pitchwise positions $y/P = -0.5$, -0.75, and -1.0 were used to prescribe the mean velocity at the inlet to the computational domain. For temperature and eddy viscosity, profiles for a turbulent boundary layer scaled to match the experimentally measured momentum thickness Reynolds number were used. As in the experiments, the freestream turbulence intensity at the inlet plane of 11% was specified, the lengthscale prescribed in the freestream (to set the freestream eddy viscosity) was set equal to roughly half of the boundary layer thickness at the inlet of the computational domain. Computations in which the freestream turbulence lengthscale was increased by one order of magnitude showed relatively little influence on endwall quantities. Previous work by Garg and Ameri [22] showed an effect of the freestream lengthscale on blade heat transfer in RANS prediction using the k–ω and SST turbulence models in a transonic cascade. Variations in the lengthscale using k–ω were attributed as the principle cause of changes in blade heat transfer. Unfortunately, k–ω is sensitive to freestream conditions, a drawback of the model, and possibly contributing to the changes observed by Garg and Ameri [22].

Zero-gradient conditions were specified at the outlet boundary. The wall-layer was resolved, i.e., the governing equations were integrated to the wall and the no-slip conditions were applied to the velocity field. The vane and hub endwall were isothermal, with the surface temperature prescribed at 311.4 K (cooler than the freestream). A zero stress condition was applied to the upper surface of the computational domain, located 207 mm from the endwall at the inlet, periodic conditions were applied along the pitchwise direction.

3. Results

The inlet to the computational domain was 170 mm upstream of the vane leading edge as illustrated in Fig. 2. Measurements of the turbulent boundary layer that were used to specify the inlet velocity field at this location are summarized in Table 2. The measured freestream velocity at the inlet plane for the three pitchwise locations summarized in Table 2 showed negligible variation, varying from 10.1 to 10.2 m/s for these locations. As shown by the table, the integral quantities obtained from the mean streamwise velocity profile increase away from Plane L1 ($y/P = -1.0$), with more than a doubling of the momentum thickness, for example. The boundary layer thicknesses tabulated above are comparable to the elevation change of the endwall resulting from axial profiling. As shown below, the relatively strong elevation change measured in terms of the boundary layer thickness results in significant differences in flow structure and surface heat transfer compared to the flat endwall reported by PSR.

Table 2
Boundary layer parameters at the inlet plane obtained from streamwise velocity measurements

y/P=	−1.00	−0.75	−0.50
Boundary layer thickness, δ_{99}	14	24	28
Momentum thickness, δ_2	1.0	1.8	2.3
δ_{99}/R	0.55	0.99	1.15
Shape factor, H	1.94	1.61	1.46
Re_{δ_2}	588	1059	1366

Dimensional quantities in mm.

3.1. Velocity measurements

Mean velocity profiles as a function of the pitchwise coordinate at two locations upstream of the vane leading edge are shown in Fig. 4a and b. Predictions and measurements of the streamwise component u and pitchwise component v are shown for two wall-normal locations, $z = 55$ mm and $z = 100$ mm; all profiles shown in Fig. 4a and b have been made dimensionless using the mixed-mean streamwise velocity, U_{avg}. The wall-normal (z) locations shown in the figure are outside the endwall boundary layer, and for both streamwise locations, Fig. 4a and b shows negligible variation between these two distances from the endwall.

In general, the measured and predicted distributions are similar. Fig. 4a shows the profiles 50 mm upstream of the vane leading edge. At this location the influence of the vanes on the velocity components is already apparent with the velocity increasing towards the suction side of the vane ($-0.4 < y/P < 0$), corresponding to the increase in u and increase (in magnitude) in v. Closer to the vane, at a streamwise location 10 mm upstream of the vane leading edge in Fig. 4b, the influence of the vanes is clearly stronger, the effects observed in Fig. 4a are accentuated—increase in the magnitude of the velocity vector towards the suction side (negative pitchwise coordinate) and a reduction towards the pressure side. Overall, the predicted velocities exhibit slightly larger peak-to-peak variation than measured.

Pitchwise distributions of the predicted and measured mean velocity magnitude at two streamwise locations downstream of the trailing edge are shown in Fig. 4c and d. For each streamwise location, two sets of profiles are shown corresponding to wall-normal locations of $z = 55$ mm and $z = 115$ mm. The velocities in Fig. 4c and d have been made dimensionless using the average value, V_{avg}, extracted from the profiles of $(u^2 + v^2)^{1/2}$. At a streamwise location 10 mm downstream of the vane

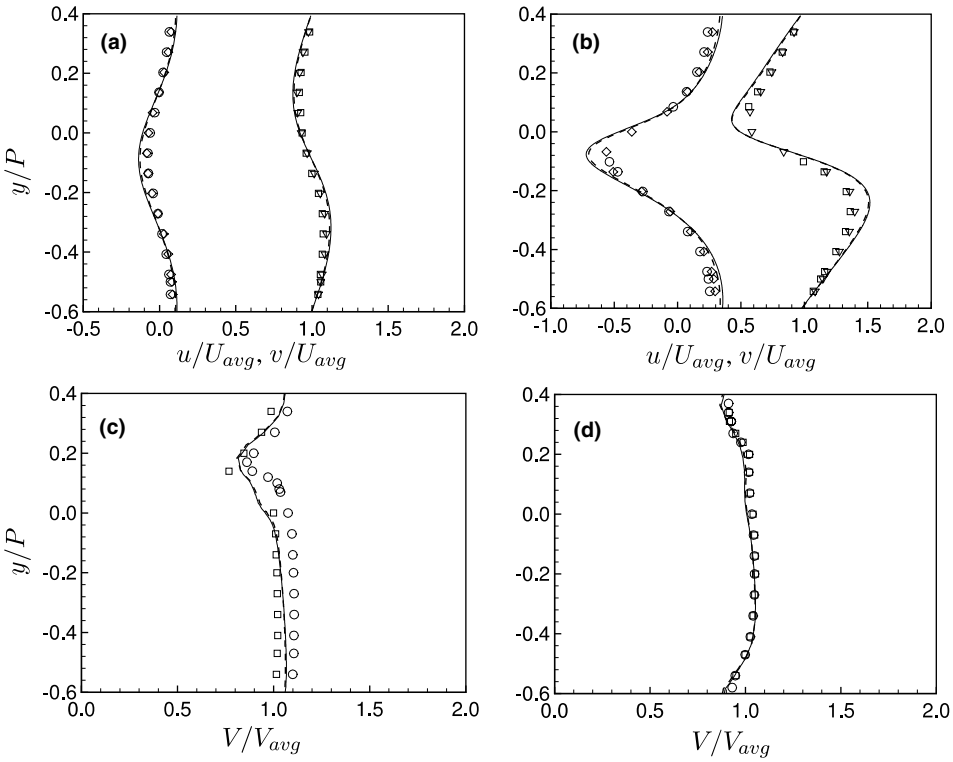

Fig. 4. Measurements (symbols) and predictions (lines) of the mean velocities. *Upper row*. Streamwise (u) velocities at $z = 55$ mm: ----, □. Streamwise (u) velocities at $z = 100$ mm: —, ▽. Pitchwise (v) velocities at $z = 55$ mm: ----, ◇ Pitchwise (v) velocities at $z = 100$ mm: —, ○. *Lower row*: vector magnitude of the mean velocity, $V = (u^2 + v^2)^{1/2}$, downstream of the vane trailing edge. At $z = 55$ mm: ----, ○. At $z = 115$ mm: —, □. (a) 50 mm upstream of the vane leading edge; (b) 10 mm upstream of the vane leading edge; (c) 10 mm downstream of the vane trailing edge; (d) 20 mm downstream of the vane trailing edge.

trailing edge, Fig. 4c shows the deficit in the velocity profile due to the wake of the vane. The measured variation in the profiles with endwall normal coordinate is more substantial in Fig. 4c than at positions upstream of the vane. The simulation result is in reasonable agreement with that measured, but shows little change with distance from the endwall. Further downstream, at a streamwise distance 20 mm from the vane trailing edge, Fig. 4d shows the increase in the width of the wake of the velocity profile (shifted to the top and bottom of the frame in the figure due to streamwise evolution). The figure again shows adequate agreement between the simulation result and measured distributions.

Fig. 5 shows measured distributions of the streamwise and pitchwise fluctuating velocities upstream of the vane leading edge and downstream of the trailing edge. The axial locations for the measured distributions are the same as the corresponding axial locations of the mean velocity profiles in Fig. 4a and b (upstream of the leading edge) and Fig. 4c and d (downstream of the trailing edge). Fig. 5 shows a difference in the development of both the freestream axial and pitchwise velocity fluctuations, with a decrease/increase in the axial/pitchwise fluctuations towards the suction (negative y/P) side of the vane and opposite behavior toward the pressure (positive y/P) side as the flow approaches the vane. As the flow accelerates towards the suction side, Fig. 5 shows that the turbulence intensities remain relatively insensitive with distance from the wall (along z). The streamwise evolution of the axial intensity is strong with an increase towards the pressure side and the axial location nearer the vane. The different evolutions of the turbulence intensities towards the pressure and suction sides is apparent in the downstream distributions in Fig. 5c and d, especially in the pitchwise component in Fig. 5d. Compared to the streamwise components in Fig. 5c, the pitchwise fluctuations in Fig. 5d are substantially larger towards the pressure side and at the location nearer the vane trailing edge (10 mm downstream from the trailing edge). Fig. 5d shows the decay in the peak values with downstream evolution.

3.2. Flow structure

In this subsection, the development of the flow through the passage is described, comparing the baseline

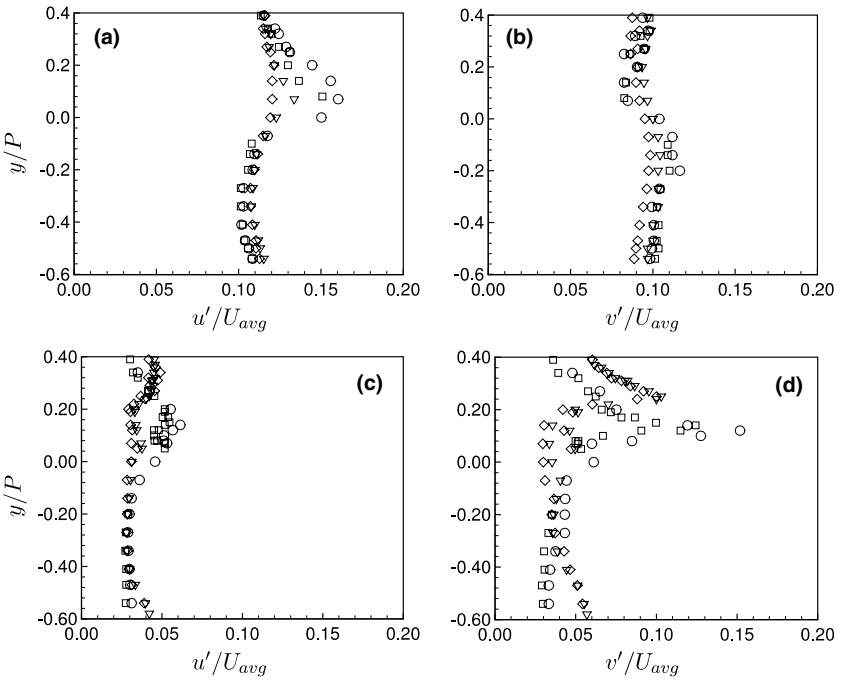

Fig. 5. Measured turbulence intensities. Upper row: 50 mm upstream of the vane leading edge: (▽) $z = 55$ mm; (◊) $z = 100$ mm. 10 mm upstream of the vane leading edge: (□) $z = 55$ mm; (○) $z = 100$ mm. Lower row: 10 mm downstream of the vane trailing edge: (□) $z = 55$ mm; (○) $z = 115$ mm. 20 mm downstream of the vane trailing edge: (▽) $z = 55$ mm; (◇) $z = 115$ mm. (a, c) Streamwise; (b, d) pitchwise intensity.

case (no secondary air injection) with that obtained for secondary air injection at a blowing ratio of 1.3 and 1.7. Properties of the solutions in three planes are presented, with the streamlines, coherent structures, and temperature used to describe the development of the flow and thermal fields. Coherent structures are identified based on the eigenvalue analysis proposed by Jeong and Hussain [16] using the symmetric tensor $S_{ik}S_{kj} + \Omega_{ik}\Omega_{kj}$ where S_{ij} and Ω_{ij} are the strain- and rotation-rate tensors, respectively. The positions of the planes for which various flow variables are extracted is shown in Fig. 2. Plane L1 is normal to the leading edge of the vane and the visualizations assist in developing insight into the rollup of the boundary layer upstream of the vane, the effect of hub-endwall axial profiling, and qualitative nature of the effect of secondary air injection. The subsequent planes (Planes S1 and S2 in Fig. 2) facilitate a description of the evolution of the vortical motion within the passage and its effect on thermal transport.

Shown in Figs. 6 and 7 are, respectively, contours of the coherent structures and temperature contours in Plane L1 for the baseline case and two blowing ratios. Particle paths in the plane are also shown in each figure. In Fig. 7 the temperature contour is shown for a dimensionless measure that ranges from the lowest value of 0 (blue) to the highest value of 1 (red). For the cases with secondary air injection the temperature contours are from computations with cooler-than-mainstream secondary air.

For the baseline flow, Figs. 6a and 7a show the rollup of vortical structures upstream of the vane leading edge, with the primary structure adjacent to the small step (slightly downstream of the flat section in the vicinity $x \approx 0.15$ and $z < 0$). This structure is the signature of the horseshoe vortex in the L1 plane which on a flat endwall would form adjacent to the vane-endwall junction. Secondary and tertiary structures are also educed deeper inside the cavity formed by the curved section and vertical face. There is a smaller structure identified near the vane-endwall junction (near $x = 0.17$ m in the figure) which has the same sense of rotation as the horseshoe vortex upstream. This smaller structure also splits into a pressure-side and a suction-side leg. Additionally, a very small and weak corner vortex (not shown in Fig. 6a) is found at the junction corner. The temperature contours in Fig. 7a show the effect of the rollup of boundary layer fluid (the primary horseshoe vortex) on the thermal field. As is well known, and demonstrated in the flat-endwall study of PSR, the horseshoe vortex and an associated small but intense corner vortex elevate heat transfer rates at the vane-endwall junction due to the transport to the endwall of hot mainstream gas by

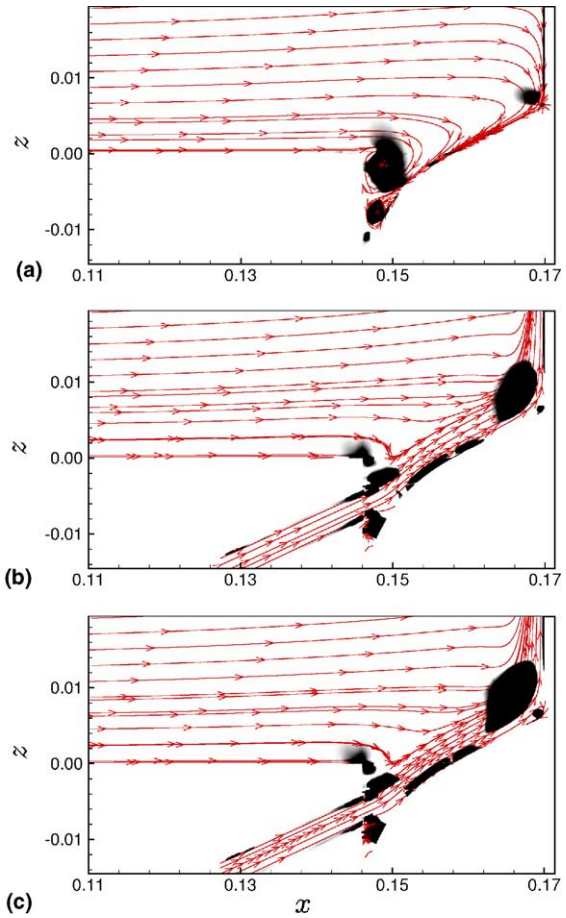

Fig. 6. Streamlines and coherent structures in Plane L1, axis dimensions in meters. (a) Baseline; (b) BR = 1.3; (c) BR = 1.7.

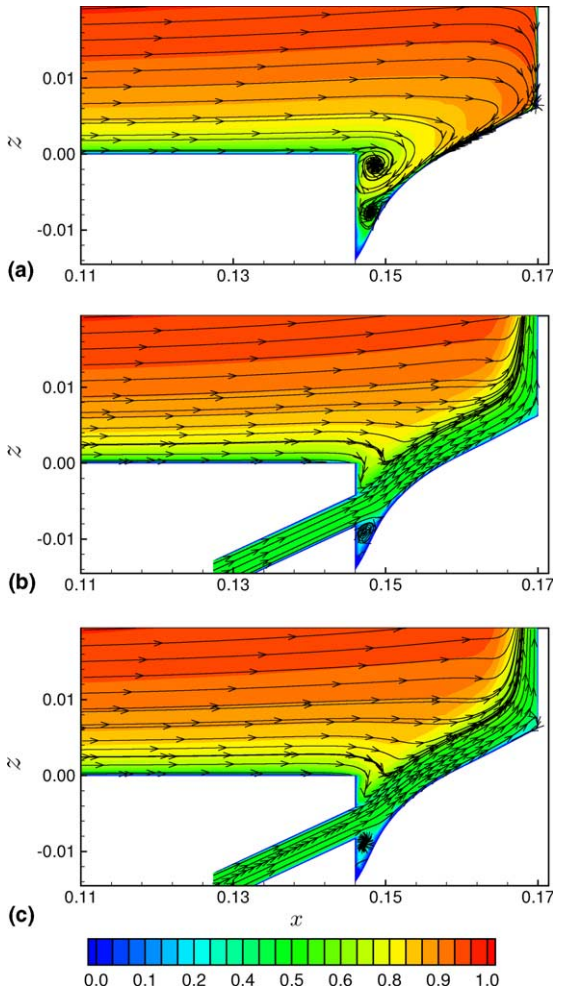

Fig. 7. Dimensionless temperature in Plane L1, $\theta = (T - T_w)/(T_\infty - T_w)$, axis dimensions in meters. (a) Baseline; (b) BR = 1.3; (c) BR = 1.7.

the vortical motions. As also discussed below, the displacement upstream of the primary vortical structure due to the axially profiled endwall lowers heat transfer rates over most of the region near the leading edge of the vane-endwall junction. Fig. 7a shows that the primary horseshoe vortex situated slightly downstream of the notch ($x \approx 0.15$) rolls up the thermal boundary layer. The smaller vortical structure educed near the vane-endwall junction ($x \approx 0.17$, $z \approx 0.005$), while possessing the same sense of rotation as the larger horseshoe vortex is not as efficient at providing a structural mechanism for transporting hotter mainstream fluid to the endwall.

The influence of secondary air injection on the coherent structures and temperature field in the Plane L1 are shown in Figs. 6b and c and 7b and c for BR = 1.3 and 1.7. In general, the effect of secondary air injection on the structural aspects of the solutions for the two blowing ratios is similar, the flow being strongly altered compared to the baseline case. The primary vortex in the baseline case that is educed slightly downstream of the step corresponds to the coherent structures in Fig. 6b and c that are educed at the corner of the step ($x \approx 0.145$, $z \approx 0$), the figures showing that in the Plane L1 the horseshoe vortex is smaller and displaced slightly upstream compared to the baseline case. Fig. 6b and c also show that a relatively large coherent structure is educed at the vane-endwall junction (slightly upstream of $x \approx 0.17$). This structure arises from the interaction of the fluid ejected from the slots with the vane and has a sense of rotation that is counter-clockwise—opposite to the sign of the vorticity of the horseshoe vortex (in Fig. 6b and c a secondary structure at the vane-endwall junction that is induced by the larger structure and from the streamlines exhibits a sense of rotation that is clock-wise). Fig. 6b and c show that this structure is too weak to roll up the mean flow streamlines, though

sufficiently intense to be identified using the eduction algorithm of Jeong and Hussain [16].

The temperature contours in Fig. 7b and c show similar effects for the two blowing ratios, with an effective "thermal shield" of cooler air over the curved section beginning from the region downstream of the slots to the vane-endwall junction. The large structure that forms at the junction as shown in Fig. 6b and c would provide a mechanism for the cooler secondary fluid to wrap around it in a counter-clockwise fashion, though Fig. 7b and c shows that this structural feature is too weak to provide visible alteration of the temperature field in the L1 plane.

In Fig. 8 are shown contours of the coherent structures and temperature in Plane S1. For the figures the abscissa is defined along the plane, i.e., the horizontal coordinate (ξ_1 in the axis label) is defined normal to the suction side of the vane (and, therefore, the view is into the passage from upstream). The coherent structures shown 8a for the baseline case show the suction- and pressure-side legs, from adjacent vanes, of the horseshoe vortices that have formed substantially upstream of the vanes (c.f., Fig. 6a). Injection of secondary air particularly distorts the suction-side leg of the horseshoe vortex (in the vicinity of $\xi_1 \approx 0.025\,\mathrm{m}$)—the pressure-side leg is also distorted but to a much lesser degree (Fig. 8b and c). Fig. 8b shows that for BR = 1.3 the suction-side leg is smaller in size compared to the baseline case. An additional increase in the blowing ratio to BR = 1.7 shows that the suction-side leg is no longer resolved in Fig. 8c. An additional difference between the structures of the baseline and blowing cases is the coherent structure educed adjacent to the suction-side of the vane in Fig. 8b and c for the blowing cases. The structure identified is due to the interaction of the secondary air with the main flow.

The temperature contours in Plane S1 follow the same scaling as for the L1 plane. Both the baseline flow

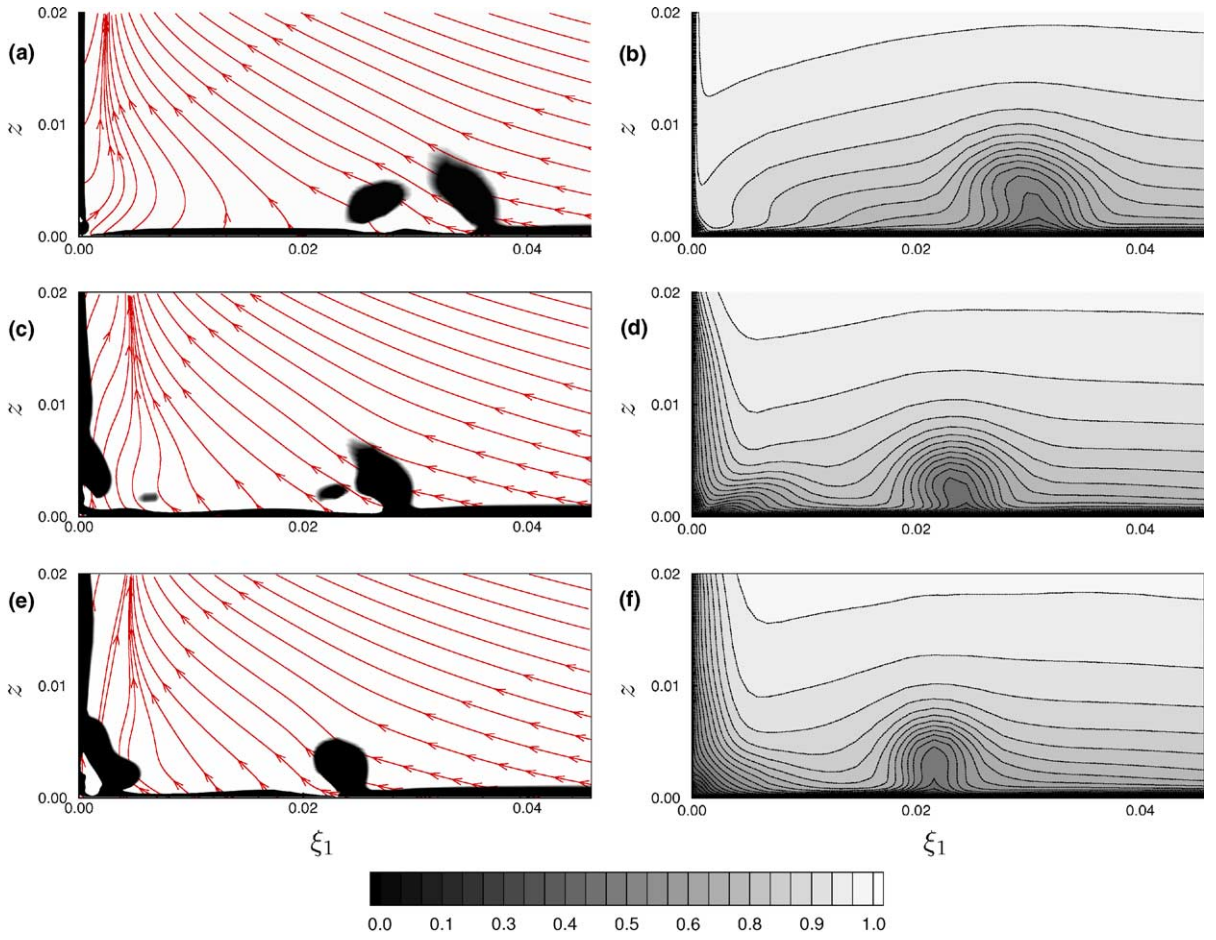

Fig. 8. Coherent structures and dimensionless temperature in Plane S1, $\theta = (T - T_w)/(T_\infty - T_w)$. View is into the passage from upstream (suction surface on the left vertical boundary of the frame), axis dimensions in meters. (a, b) baseline; (c, d) BR = 1.3; (e, f) BR = 1.7.

and blowing cases show a "bulge" of lower temperature fluid near the middle of the passage that has been lifted from the endwall by the interaction of the counter-rotating vortical structures (the pressure- and suction-side legs of horseshoe vortices from adjacent vanes). The common flow between the structures is away from the endwall, this in turn providing the mechanism to lift cooler fluid from the endwall, and into the passage. Fig. 8d and f show that for the blowing cases there is a similar lifting of cooler fluid from near the endwall into the passage as occurs in the baseline case (Fig. 8b). Fig. 8 also shows that a significant effect of the secondary air injection on the temperature field occurs near the suction side of the vane, with a region of lower temperature fluid along the vane suction side (the figure corresponds to a case with cooler secondary air).

3.3. Hub endwall heat transfer characteristics

Comparison of heat transfer characteristics against experimental measurements is achieved using the endwall distributions of the Stanton number, St, and cooling effectiveness, η. These quantities for the secondary air injection cases are defined as

$$St = \frac{q''_w}{\rho U_\infty c_p (T_r - T_w)}, \quad \eta = \frac{T_\infty - T_r}{T_\infty - T_s}, \tag{1}$$

where ρ and c_p represent the fluid density and specific heat, respectively. The freestream velocity and freestream temperature are denoted U_∞ and T_∞ in (1), respectively, T_r is the reference temperature (i.e., the adiabatic wall temperature), q''_w is the heat flux into the wall, and T_s is the temperature of the secondary air injected through the slots. The wall temperature is denoted T_w in (1). To obtain St and η for the solution with secondary air injection, two computations were performed, the first with "hot" secondary air, i.e., at a temperature above the mainstream air and a second calculation with "cold" secondary air at a temperature below that of the mainstream air. For the baseline case without air injection, the Stanton number is defined as usual with the reference temperature equal to the freestream temperature in (1).

Measurements and predictions of the Stanton number and cooling effectiveness on the hub endwall are presented in Figs. 9 and 10, respectively. For the baseline case, the general characteristics observed in Fig. 9 are: levels in the vicinity of the leading edge around

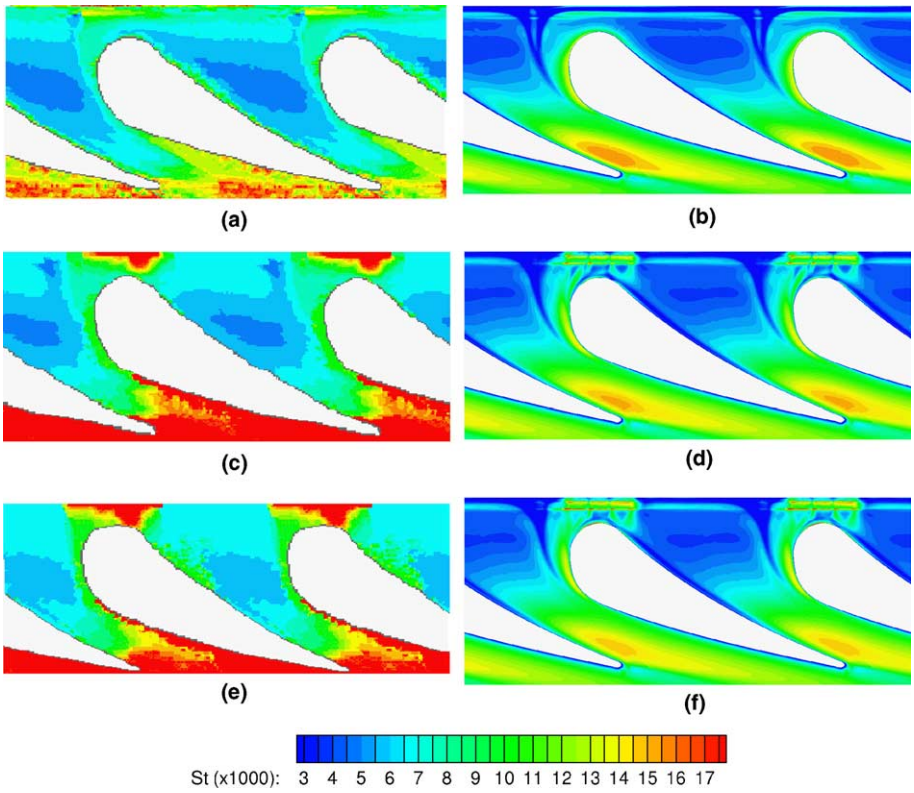

Fig. 9. Endwall Stanton number. Measured distributions shown in left column, predicted distributions shown in right column. (a, b) baseline configuration; (c, d) BR = 1.3; (e, f) BR = 1.7.

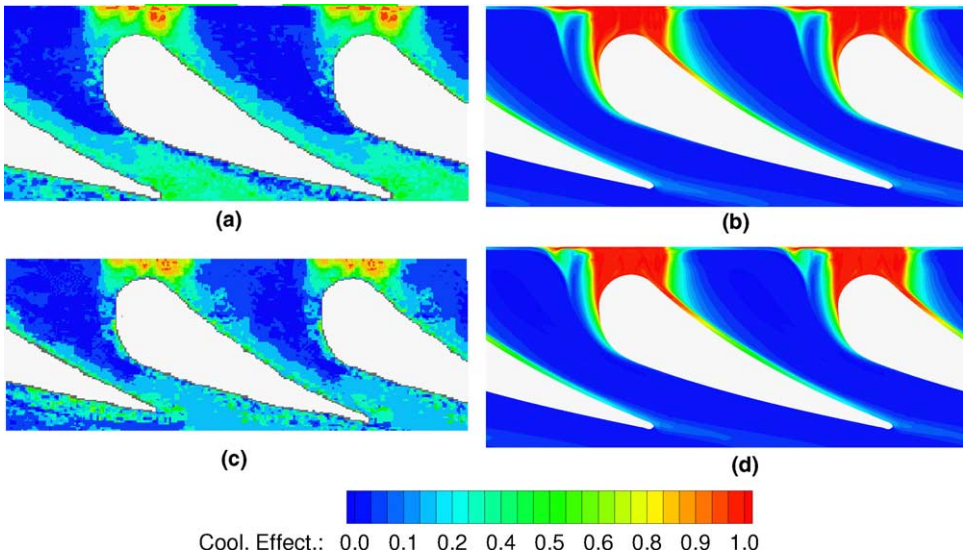

Fig. 10. Endwall cooling effectiveness. Measured distributions shown in left column, predicted distributions shown in right column. (a, b) BR = 1.3; (c, d) BR = 1.7.

$St \approx 0.011$, approximately the same level in a narrow region adjacent to the vane pressure surface, and a higher level (≈0.013–0.015) in the downstream half of the passage toward the suction surface. Consistent with the description of the flow field given earlier, flow reversal rolls up boundary layer fluid upstream of the vane, the endwall axial profiling preventing the main horseshoe vortex structure from developing directly adjacent to the leading edge. This in turn limits the efficiency of the structure in transporting hot mainstream gas to the hub endwall as occurs for the flat endwall case and shown in PSR. The small crescent-shaped region of modestly high *St* (also 0.010–0.011) in the vicinity of the leading edge arises from the weaker, compared to the flat endwall case, vortical structure (also a horseshoe vortex, albeit a weaker one) at the vane-endwall junction. The lowest measured Stanton numbers in the passage occur upstream of the throat, around 0.004–0.005, increasing as the flow accelerates, thinning the boundary layer, through the minimum flow area between the vanes.

The predicted *St* distribution around the leading edge of the vane and into the suction side (Fig. 9b) agrees reasonably well with measurements (Fig. 9a) for the baseline case. As also observed in the measured distribution, a thin region of higher *St* along the suction side, downstream of the leading edge and upstream of the throat, is predicted by the simulation. The largest differences between the simulation and experiment occur further downstream, with lower *St* predicted than measured near the vane suction surface, and higher *St* predicted than measured near the pressure side close to the trailing edge. A probable source of the discrepancies in these regions is modeling errors associated with both the velocity and thermal fields. Pressure gradient changes in the flow are strong, challenging the turbulence model and ability of the calculation to accurately predict boundary layer growth. In addition, the turbulent heat flux is closed by invoking Reynolds analogy presuming that similar mechanisms govern the turbulent transport of momentum and heat. However, pressure contributions to the transport of the mean and fluctuating velocities that do not appear in the transport equation for the thermal field are an important difference given the strong changes in the freestream. This would in turn be expected to lead to inaccuracies in the thermal field prediction using models that employ a turbulent Prandtl number. In spite of the simplified model for heat transfer, Fig. 9 does indicate that the predicted overall features of the *St* distribution are not unreasonable.

Stanton number and cooling effectiveness for the blowing cases are shown in Figs. 9c–f and 10, respectively. Comparison of the measurements and simulations shows a relatively weak change in *St* and η with changes in the blowing ratio from 1.3 to 1.7. Slightly downstream of the slots and upstream of the vane leading edge, the Stanton number is higher in the region close to the injection locations compared to the baseline case. However, in this region, the cooling effectiveness is close to unity. As already discussed, the local surface heat flux, which is a function of both the Stanton number and the cooling effectiveness, is the important quantity vis-a'-vis the local thermal state of the surface. The

blowing of cooler secondary air does serve to reduce the heat flux in this region. An influence of blowing on the measured endwall Stanton number is observed in the downstream half of the passage, particularly toward the suction side—*St* is elevated to 0.015–0.017. A similar increase occurs near the pressure side close to the vane trailing edge. Again, the measured cooling effectiveness in these regions is significant (0.4–0.6), with its accompanying beneficial effect. The corresponding predicted *St* values are somewhat lower (0.013–0.015). The predicted η values are substantially lower—about 0.1 over most of this half of the endwall and between 0.2 and 0.3 in a thin region adjacent to the vane pressure surface. These values of η are not insignificant however—some reductions in the surface heat flux can be expected to occur. Nevertheless, the predictions are not nearly as successful in the downstream half of the passage as in the upstream half.

3.4. Total pressure loss coefficient

The total pressure loss coefficient was measured and comparisons of simulation results against the data are presented in this section. The total pressure loss coefficient is defined as

$$C_{p0} = \frac{P_{0,\text{inlet}} - P_0}{\rho U_\infty^2/2}, \tag{2}$$

where P_0 is the total pressure and ρ and U_∞ are the free-stream density and velocity, respectively, at the inlet plane. Predicted contours of the total pressure coefficient in Plane S1 and vorticity normal to Plane S1 are shown in Fig. 11. Results are shown for the baseline case and each blowing ratio. The general behavior illustrated in Fig. 11 is the correlation between the region of elevated values in the total pressure loss coefficient and the counter-rotating structures in Plane S1. In general, the figures

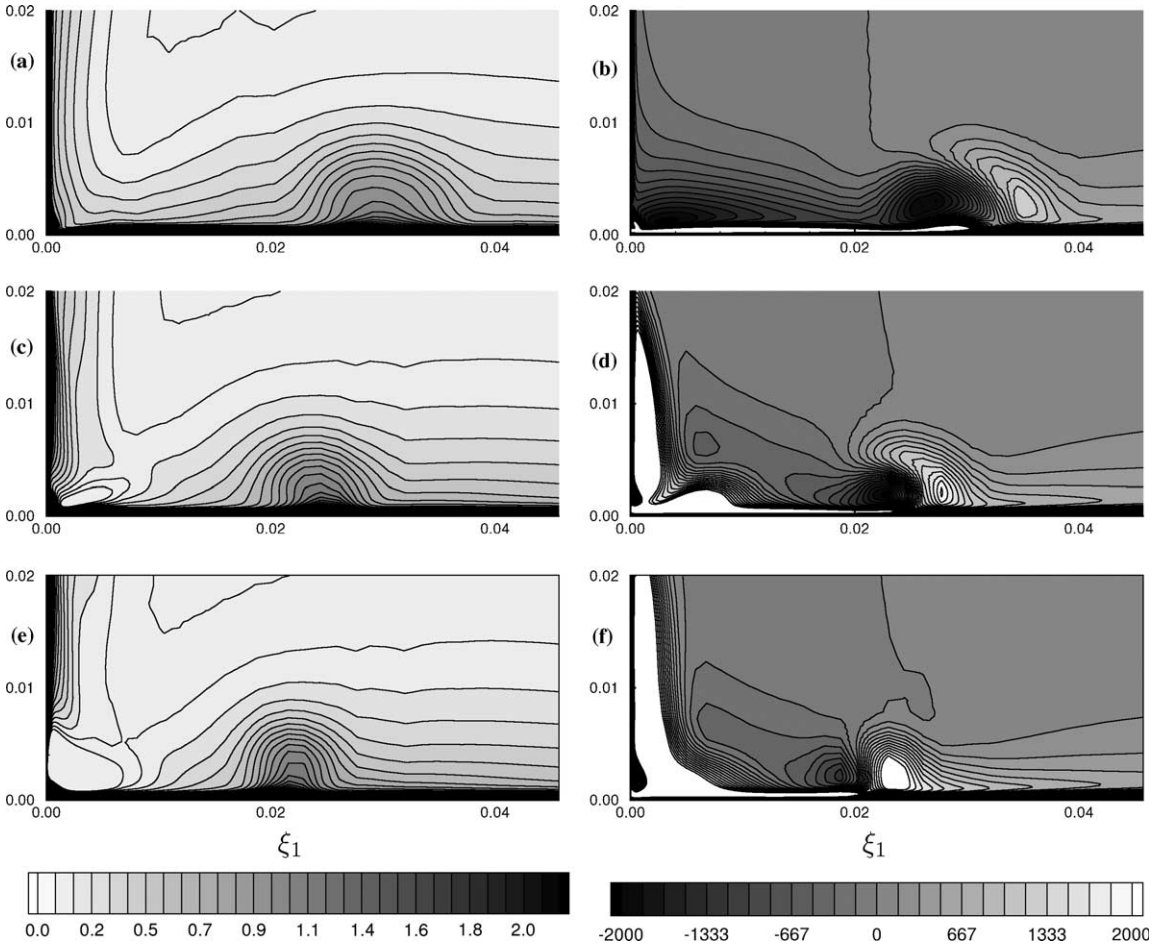

Fig. 11. Predicted total pressure loss coefficient (left frames) and normal vorticity (right frames) in Plane S1. View is from upstream into the passage, axis dimensions in meters. (a, b) baseline case, (c, d) BR = 1.3, (e, f) BR = 1.7.

also show that increase in the blowing ratio from 1.3 to 1.7 does not substantially alter the shape or values of the total pressure loss coefficient (c.f., Fig. 11c and e), though the corresponding contours of the normal vorticity in Fig. 11d and f are somewhat more strongly influenced by blowing. The suction side leg of the horseshoe vortex (at $\xi_1 > 0.02$ in the vorticity plots) is less intense with increase in blowing. For both blowing ratios the figure also shows that the location of the structure in the plane is nearer the suction surface compared to the baseline case.

The total pressure loss coefficient was measured at two axial planes, Planes 4 and 5 in Fig. 1. Model predictions are compared to the measurements in Figs. 12 and 13 for Plane 4 and Plane 5, respectively. The y' (Plane 4) and y'' (Plane 5) axes originate at the vane suction surface. Both measurements and simulations show that the size of the loss core grows as the flow evolves downstream, with measured maxima in C_{p0} increasing from around 10 in Plane 4 to about 12 in Plane 5. Qualitatively, the loss core in the simulation is similar to that measured, though peak values of C_{p0} are higher than in the experiments, e.g., maxima in the simulations in Plane 5 are around 14.

Measurements indicate that secondary air injection results in less change in C_{p0}, both within the passage in Plane 4 and downstream in Plane 5, than predicted by the simulations. Both the size of the loss core and approximate location of the "eye" of the structure corresponding to the highest C_{p0} are altered less by blowing

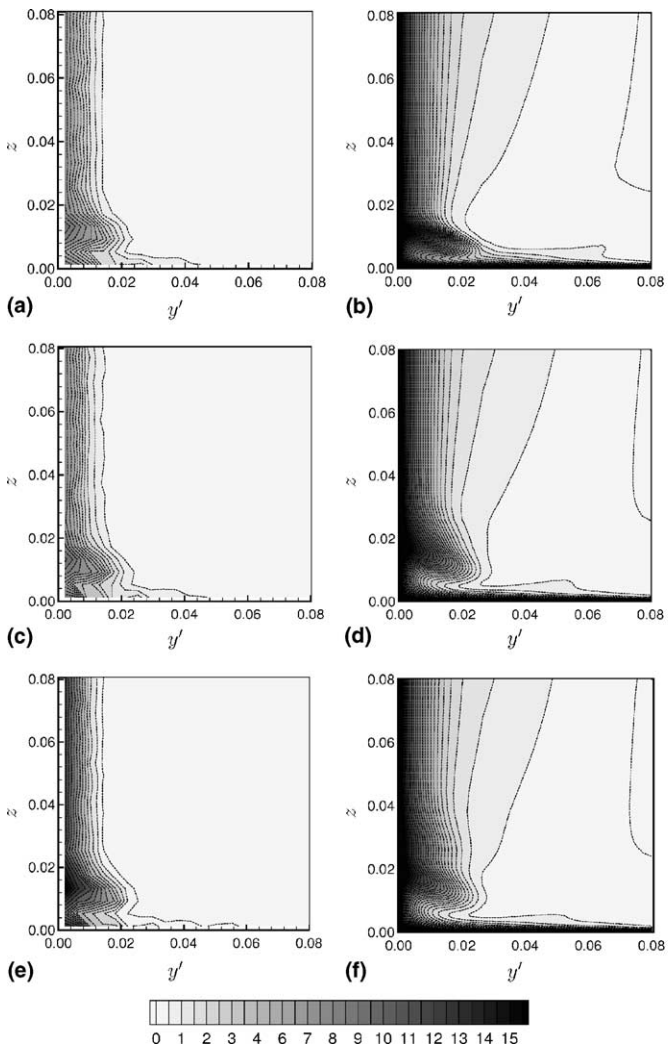

Fig. 12. Total pressure loss coefficient C_{p0} in Plane 4. View is from upstream into the passage. Measured values in the left frames, predictions in the right frames. Axis dimensions in meters. (a, b) baseline; (c, d) BR = 1.3; (e, f) BR = 1.7.

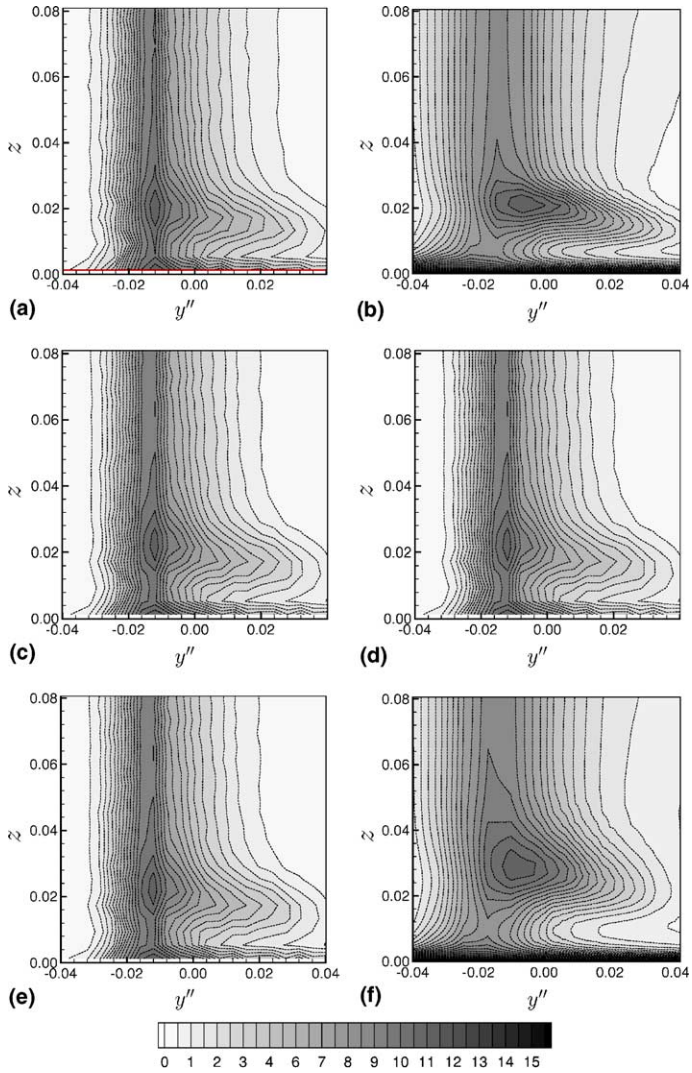

Fig. 13. Total pressure loss coefficient C_{p0} in Plane 5. View is from upstream into the passage. Measured values in the left frames, predictions in the right frames. Axis dimensions in meters. (a, b) baseline; (c, d) BR = 1.3; (e, f) BR = 1.7.

than can be observed in the simulations. The simulations show the loss core undergoes a more substantial change as the blowing ratio is increased from 1.3 to 1.7, through stronger effects of blowing, with the loss core lifted further away from the endwall as secondary air injection is increased. The agreement between simulation and measurement in Fig. 13 is adequate, one of the main differences being the relatively more diffuse region of non-zero C_{p0}, though the level of the maximum values are in reasonable agreement. For the cases with secondary air injection, the structure defining C_{p0} is further from the wall compared to the baseline case, a slight upward shift also evident in Fig. 13 with increases in blowing ratio in the simulations.

4. Summary

The flow and heat transfer in a linear cascade of turbine vanes were investigated using a combination of numerical simulation and laboratory experiments. Measurements of the Stanton number and cooling effectiveness were obtained on the axially profiled hub endwall for flows with prescribed secondary air injection—a baseline case with no injection, and two cases with blowing ratios of 1.3 and 1.7. Total pressure measurements were used to provide some detail relating to the structure of the flow and the influence of secondary air injection on losses within the passage. The velocity and thermal field were predicted via solution of the Rey-

nolds-averaged Navier–Stokes equations using the Spalart–Allmaras one-equation model to close the turbulent Reynolds stress. The turbulent heat flux was closed using a constant turbulent Prandtl number of 0.9.

For the configuration studied, the inflow boundary layer thickness and elevation change of the hub endwall are comparable. Flow visualizations from the calculations show that the axial profiling is sufficient to lead to flow reversal significantly upstream of the vane leading edge, with a horseshoe vortex formed farther upstream of the vane compared to that occurring on a flat endwall. This feature in turn appears to be the mechanism preventing transport of mainstream air to the vane-endwall junction. The horseshoe vortex structure develops further into the passage, with a "bulge" of low-temperature fluid lifted from the endwall and into the mainstream of the passage. Secondary air injection strongly distorts the flow—while the upstream boundary layer rolls up into a horseshoe vortex as in the baseline case, fluid ejected from the slots develops into a relatively large coherent vortical structure at the vane-endwall junction, but with a sense of rotation opposite to that of the upstream boundary layer vorticity.

For the turbulence model, the present flow combines effects of strong pressure gradients, streamline curvature, heat transfer, and freestream turbulence. Each of these factors continue to challenge RANS turbulence models. Freestream treatment is especially subtle since *ad hoc* adjustment of turbulence variables (e.g., turbulence kinetic energy and a lengthscale in two-equation models) to match experimental measurements, for example, does not necessarily imply a closer connection of the model to the physics. Given these features, the overall aspects of the computation are in many respects encouraging. Predictions of surface transfer characteristics, for example, are not unreasonable in many regions of the endwall. In the passage, the primary flow diagnostic was measurement of the total pressure loss coefficient. Comparison in the passage and along planes near the trailing edge of the vane showed similar qualitative features, but with model predictions of losses higher than those measured. One contributor to the over-predictions of the total pressure loss coefficient is the use of the Spalart–Allmaras model without corrections for streamline curvature. Curvature corrections would reduce the eddy viscosity, an effect that would lower dissipation and possibly improve prediction of losses. in general, attempts at incorporating improvements to existing RANS models such as S-A using, for example, non-linear constitutive relations would appear worthwhile. Such investigations are also motivated with a view towards the longer term and the development of simulation strategies for predicting flows that are inherently time dependent and for which direct resolution of a portion of the turbulent eddies is desirable. New simulation strategies for such applications that are based on combination of RANS approaches with Large Eddy Simulation are under intense development and may have a useful role in modeling components of gas turbine engines. The steady-state RANS investigations reported in this manuscript provide a useful baseline for assisting in the interpretation of other simulation approaches for such complex flows with heat transfer.

Acknowledgment

The authors gratefully acknowledge the support of the National Science Foundation, Thermal Transport and Thermal Processing Program, Division of Chemical and Thermal Systems, under grant number CTS-9904172 as well as Honeywell Engines and Systems, Phoenix, Arizona. Thanks are due to Dr. S. Kang for his measurements of the velocity field.

References

[1] M.G. Dunn, Convective heat transfer and aerodynamics in axial flow turbines, ASME J. Turbomachinery 123 (2001) 637–686.
[2] A. Yamamoto, Y. Kondo, R. Murao, Cooling-air injection into secondary flow and loss fields within a linear turbine cascade, ASME J. Turbomachinery 113 (1991) 375–383.
[3] J.H. Leylek, R.D. Zerkle, Discrete-jet film cooling: a comparison of computational results with experiments, ASME J. Turbomachinery 116 (1994) 358–368.
[4] K.T. McGovern, J.H. Leylek, A detailed analysis of film cooling physics. Part II: compound-angle injection with cylindrical holes, ASME J. Turbomachinery 122 (2000) 113–121.
[5] I.S. Jung, J.S. Lee, Effects of orientation angles on film cooling over a flat plate: boundary layer temperature distributions and adiabatic film cooling effectiveness, ASME J. Turbomachinery 122 (2000) 153–160.
[6] G. Wilfert, S. Wolff, Influence of internal flow on film cooling effectiveness, ASME J. Turbomachinery 122 (2000) 327–333.
[7] C.A. Hale, M.W. Plesniak, S. Ramadhyani, Film cooling effectiveness for short film cooling holes fed by a narrow plenum, ASME J. Turbomachinery 122 (2000) 553–557.
[8] A. Duden, I. Raab, L. Fottner, Controlling the secondary flow in a turbine cascade by 3D airfoil design and endwall contouring, ASME Paper 98-GT-72, 1998.
[9] A. Duden, L. Fottner, The secondary flow field of a turbine cascade with 3D airfoil design and endwall contouring at off-design incidence, ASME Paper 99-GT-211, 1999.
[10] S.W. Burd, T.W. Simon, Effects of slot bleed injection over a contoured endwall on nozzle guide vane cooling performance. Part II: thermal measurements, ASME Paper 2000-GT-200, 2000.
[11] N.W. Harvey, M.G. Rose, M.D. Taylor, S. Shahpar, J. Hartland, D.G. Gregory-Smith, Nonaxisymmetric turbine end wall design. Part II: three-dimensional linear design system, ASME J. Turbomachinery 122 (2000) 278–285.

[12] J.C. Hartland, D.G. Gregory-Smith, N.W. Harvey, M.G. Rose, Nonaxisymmetric turbine end wall design. Part II: experimental validation, ASME J. Turbomachinery 122 (2000) 286–293.
[13] R.A. Oke, S.W. Burd, T.W. Simon, Film-cooling experiments with flow introduced upstream of a first stage nozzle guide vane through slots of various geometries, ASME Paper GT-2002-30169, 2002.
[14] F.E. Ames, P.A. Barbot, C. Wang, Effects of aeroderivative combustor turbulence on endwall heat transfer distributions acquired in a linear vane cascade, ASME Paper GT-2002-30525, 2002.
[15] H. Pasinato, K.D. Squires, R.P. Roy, Assessment of Reynolds-averaged turbulence models for prediction of the flow and heat transfer in an inlet vane-endwall passage, ASME J. Fluids Eng. 126 (2004) 305–315.
[16] G. Jeong, F. Hussain, On the identification of a vortex, J. Fluid Mech. 285 (1995) 69–94.
[17] P.R. Spalart, S.R. Allmaras, A one-equation turbulence model for aerodynamic flows, La Recherche Aérospatiale 1 (1994) 5.
[18] V. Yakhot, S.A. Orszag, S. Tangham, T.B. Gatski, C.G. Speziale, Development of turbulence models for shear flows by a double expansion technique, Phys. Fluids 7 (1991) 1510–1520.
[19] B.E. Launder, G.J. Reece, W. Rodi, Progress in the development of a Reynolds-stress turbulence closure, J. Fluid Mech. 68 (1975) 537–566.
[20] Fluent, Inc., Computational Fluid Dynamics Software, Release 6.0, Lebanon, New Hampshire, 2002.
[21] J.P. van Doormal, G.D. Raithby, Enhancements of the SIMPLE method for predicting incompressible fluid flow, Numer. Heat Transfer 7 (1984) 147–163.
[22] V.K. Garg, A.A. Ameri, Two-equation turbulence models for prediction of beat transfer on a transonic turbine blade, Int. J. Heat Mass Transfer 22 (2001) 593–602.